TEL AVIV UNIVERSITY

The Iby and Aladar Fleischman Faculty of Engineering

The Zandman-Slaner School of Graduate Studies

Dense Ultrasonic Thermometry

A thesis submitted toward the degree of

Master of Science in Biomedical Engineering

by

Tal Grutman

July 23

TEL AVIV UNIVERSITY

The Iby and Aladar Fleischman Faculty of Engineering

The Zandman-Slaner School of Graduate Studies

Dense Ultrasonic Thermometry

A thesis submitted toward the degree of

Master of Science in Biomedical Engineering

by

Tal Grutman

This research was carried out in the Department of Biomedical Engineering

Under the supervision of Dr. Tali Ilovitsh

July 23

Acknowledgments

I would like to thank Dr. Tali Ilovitsh, my supervisor and mentor, for her support and leadership of this project. Thank you for giving me the opportunity to pursue my academic interests while challenging me and guiding me along the way. I am grateful and fortunate for the role you took in shaping the direction of my research and career.

Thank you also to my wife, family and friends who always encouraged me, supported me, and tried their best to understand my research.

Abstract

We developed a dense algorithm for calculating the speed-of-sound shift between consecutive acoustic acquisitions as a noninvasive means to evaluating temperature change during thermal ablation. The dense speed-of-sound shift imaging (DSI) algorithm was developed to simultaneously incorporate information from the entire field of view using a combination of dense optical flow and inverse problem regularization, thus speeding up the calculation and introducing spatial agreement between pixels natively. Thermal ablation monitoring consisted of two main steps: pixel shift tracking using Farneback optical flow, and mathematical modeling of the relationship between the pixel displacement and temperature change as an inverse problem to find the speed-of-sound shift. A calibration constant translates from speed-of-sound shift to temperature change.

The method performance was tested in ex-vivo samples and compared to standard thermal strain imaging (TSI) methods. Using a temperature sensor as a ground truth, the algorithm was applied to ex-vivo chicken samples imaged by an L12-5 imaging transducer during thermal ablation therapy. Temperature changes between 3-15ºC was measured with high thermometry precision of less than 2ºC error for temperature changes as low as 8ºC. The DSI method outperformed standard TSI in both spatial coherence and runtime in HIFU-induced hyperthermia. In conclusion, DSI can successfully monitor the speed-of-sound shift introduced by thermal ablation. This technique is faster and more robust than current methods, and therefore can be used as a noninvasive, real time and cost-effective thermometry method, with high clinical applicability

Contents

Acknowledgments III
Abstract IV
Contents V
Abbreviations and symbols VII
Figure List VIII
Table List VIII
List of Publications IX
1. Introduction 1
2. Research objectives 2
3. Theoretical background 3
3.1 Ultrasound imaging principles 3
3.1.1 Sound wave propagation 3
3.1.2 Imaging Applications 5
3.2 Therapeutic ultrasound 8
3.3 Ultrasound Safety 9
3.4 HIFU guidance 9
3.4.1 Current state-of-the-art 9
3.4.2 Thermal strain imaging 10
3.4.3 Proposed method 12
4. Materials and methods 15
4.1 Ultrasound setup 15
4.2 Post-processing 17
5. Results 18
5.1 Simulated data 18
5.2 Ex-vivo 20
5.3 Temperature estimation 22

5.4 Performance benchmark 23
6. Discussion 23
7. References 27
8. תקציר 32

Abbreviations and symbols

US	Ultrasound
HIFU	High-intensity focused ultrasound
USgFUS	Ultrasound guided focused ultrasound
A-mode	Amplitude mode
B-mode	Brightness mode
TSI	Thermal strain imaging
DSI	Dense speed-of-sound shift imaging
SNR	Signal-to-noise ratio
FWHM	Full-width at half-max
TIS	Thermal index for soft tissue
$t\ [sec]$	Time
$z\ [mm]$	Axial depth
$c\ [\frac{m}{sec}]$	Speed-of-sound
$dt\ [sec]$	Time delay
$c_0\ [\frac{m}{sec}]$	Assumed speed-of-sound in soft tissue
$T_0\ [℃]$	Initial temperature
$\delta T\ [℃]$	Change in temperature
$\beta\ [\frac{mm}{℃}]$	Thermal expansion coefficient
$\Delta\underline{d}\ [mm]$	Pixel shift
$\Delta\underline{v}\ [\frac{sec}{mm}]$	Slowness deviation
$\Delta\underline{\hat{v}}\ [\frac{sec}{mm}]$	Estimated slowness deviation
M	Integration matrix
Γ	Regularization coefficient
$\theta\ [°]$	Steering angle

Figure List

Figure 1. Dynamic beam focusing in ultrasound……6
Figure 2. Coherent plane wave compounding……7
Figure 3. DSI algorithm flow……15
Figure 4. Experimental setup……16
Figure 5. Results in simulated data…...……19
Figure 6. Ex-vivo algorithm comparison……..……20
Figure 7. Effect of treatment duration on DSI..……21
Figure 8. Temperature estimation……..……23

Table List

Table 1. Temperature effects……..……9
Table 2. Focal slowness deviation……22

List of Publications

Articles

1. **T. Grutman** and T. Ilovitsh, "Dense Ultrasonic Thermometry," in *Physics in Medicine and Biology* (Under review). Analyzed the mathematical basis of the method, implemented the code, performed experiments and data analysis, wrote the paper.
2. D. Schein, **T. Grutman** and T. Ilovitsh, "Deep Learning-Based Ultrasound Beam Shaping for Spatiotemporal Acoustic Holograms Generation," in *IEEE Transactions on Ultrasonics, Ferroelectrics, and Frequency Control*, vol. 70, no. 6, pp. 551-561, June 2023, doi: 10.1109/TUFFC.2023.3264580. Contributed to the planning of deep learning architecture and loss function.
3. T. Mano, **T. Grutman**, and T. Ilovitsh, "Microfluidic-inspired platform for ultrasound localization microscopy of bifurcating vessels" (Under review). Wrote the original data analysis code as well as Vantage acquisition protocol.

Conference Presentations

1. **T. Grutman** and T. Ilovitsh, Dense ultrasonic speed-of-sound shift imaging for thermal ablation monitoring. International Symposium on Therapeutic Ultrasound. Lyon, France, April 2023. Student poster award finalist.
2. T. Mano, **T. Grutman** and T. Ilovitsh, Flow characterization in branching vessels using a microfluidic-inspired phantom and ultrasound localization microscopy. International Symposium on Therapeutic Ultrasound. Lyon, France, April 2023. Wrote the original data analysis code as well as Vantage acquisition protocol.

Patent Applications

1. **T. Grutman** and T. Ilovitsh, "Dense Speed of Sound Shift Imaging," US Patent Application No. 63/459,216

1. Introduction

High-intensity focused ultrasound (HIFU) utilizes concentrated ultrasound waves to generate therapeutic effects in a non-invasive manner. Thermal ablation and hyperthermia are applications where ultrasound is used to precisely target and deliver high focused energy in order to achieve localized heating of the targeted areas. This focused energy can effectively destroy tumors, making HIFU a valuable option for cancer treatment, especially for prostate, liver, and breast cancer [1]–[3]. Additionally, HIFU shows potential in non-oncological applications, such as reducing chronic pain, ablation of uterine fibroids and treatment of certain neurological disorders [4]–[7]. Hyperthermia has been used in various applications of brain tumor and carcinoma treatment as well as drug delivery[8]–[11]. HIFU for thermal ablation and hyperthermia offers a precise and targeted approach, minimizing damage to surrounding healthy tissues, and often requiring minimal recovery time.

As energy is released into the tissue and the local thermal dose rises, it is crucial to monitor and guide these treatments, to make sure that the target temperature is reached at the desired locations, with minimal off-target effects to surrounding healthy tissue. Magnetic resonance imaging (MRI) thermometry is the most widely used technique for HIFU-guidance [12], [13], but the use of MRI for guiding HIFU procedures presents challenges in terms of accessibility, equipment compatibility, patient positioning, and treatment time. Ultrasound-guided focused ultrasound (USgFUS) is an emerging adaptable alternative to MRI guidance due to the advantages of ultrasound in accessibility, real-time imaging, cost-effectiveness, and versatility. Ultrasound can provide continuous visualization for precise targeting and adjustments during the procedure. This real-time feedback is obtained by imaging the local change in sound speed due to a HIFU-induced temperature change and can enhance the accuracy and delivery of

focused ultrasound energy. In this work, we developed a dense speed-of-sound shift imaging (DSI) method for temperature estimation and test our results in simulated and ex-vivo data compared to thermal strain imaging (TSI), the current state-of-the-art. Our results show a significant performance boost compared to TSI, without the need for additional post processing.

2. Research objectives

The overall goal of this work is to develop a more accurate and reliable noninvasive ultrasound imaging-based thermometry algorithm to monitor thermal-ablation treatments. TSI, the current standard for ultrasonic thermometry, uses pixel-wise block matching, which is a sparse algorithm. Neighboring pixels will not necessarily have similar output, and heavy image processing is incorporated to accommodate for this [14], [15]. To improve reliability, we turned to dense estimation techniques. Making use of spatial regularization priors, we solve the speed-of-sound shift inverse problem in a way that inherently includes local pixel coherence. The resulting speed-of-sound shift is smooth, as expected from a focused, localized procedure.

Next, we wanted to improve the processing time, which is a major drawback of current USgFUS techniques. We analyzed the computation bottleneck in the current approach and optimized our solution based on our findings. Overall, we achieved an improvement of x20 speed up in processing.

Finally, we needed to compare our results with current solutions and show that we successfully improved reliability and calculation time without lowering the final temperature estimation accuracy. To assess the ability of our algorithm to localize a HIFU focal point, we first performed a simulation replicating the effects of a speed-of-sound change in ultrasound

images acquired from an agarose phantom. Next, we evaluated the localization quality of the algorithm on ex-vivo chicken breast samples. Temperature estimation was also performed and compared to a real thermocouple reading. To compare our algorithm to the state-of-the-art, we implemented TSI as it is described in the literature and evaluated its performance compared to our algorithm for each of the experiments.

3. Theoretical background

Our DSI algorithm incorporates various concepts in ultrasound imaging and is designed to work in unison with a therapeutic ultrasound setup. In this section, we will describe the basics of ultrasound imaging necessary for DSI. Next, we will describe HIFU procedures and image-based guidance, before combining these concepts to realize the DSI algorithm.

3.1 Ultrasound imaging principles

Ultrasound imaging is conceptually similar in nature to classic imaging in the field of electromagnetic optics. Many advanced concepts in ultrasound such as beam shaping [16], multiplexing [17], [18], and ultrasound localization microscopy [19] are parallels of fields in optics. Still, there are some differences between the fields, and in this section we will describe the usage of acoustic wave based image formation.

3.1.1 Sound wave propagation

Ultrasound describes sound (pressure) waves at frequencies exceeding the audible limit of human hearing of 20 kHz. It has transformed into a major imaging modality thanks to a few unique principles of sound waves. First, sound waves are non-ionizing and safe for general imaging, although beyond a certain energy threshold, they can be utilized to induce thermal

ablation in tissue. Second, biological tissue is an excellent conductor of ultrasound, so sound waves can easily propagate through the body. Finally, the speed-of-sound in soft tissue allows sound waves to travel to and from a source fast enough for rapid imaging, and as a result ultrasound benefits from very high temporal resolution.

An ultrasound wave is usually generated by a piezoelectric element. Piezoelectric crystals have a unique property that electrical currents cause them to vibrate, releasing a sound wave. In addition, when a sound wave is absorbed by a piezoelectric crystal, the vibration induces a voltage drop. As a result, piezoelectric elements can be used for sending and receiving ultrasound waves according to arbitrary pulse sequences in the form of electrical voltage. Arrays of piezoelectric elements are combined to create an ultrasound transducer aperture, which can be used to generate more complex waves across a larger viewing field by harmonizing the piezoelectric effect across multiple coherent elements.

In pulse-echo ultrasound, a pressure wave is emitted by the transducer. Immediately afterward, the transducer begins to digitize echoes of the propagating wave as it encounters reflectors and scatterers in the medium. In a homogeneous medium with speed-of-sound c located at axial distance z from the transducer, the round-trip time of the echo is simply given by:

$$t = \frac{2z}{c} \tag{1}$$

The echo time t is linearly related to the distance from the transducer, so the time axis effectively encodes the axial distance to the scatter with amplitude recorded at time t.

In biomedical ultrasound applications, the field-of-view is almost never homogeneous, and Equation (1) must be adapted to consider heterogeneous tissue with varying sound speeds.

$$t = 2\int_0^z \frac{dz'}{c(z')} \tag{2}$$

However, the exact speed-of-sound along the propagation path is rarely known, so Equation (1) is used with a constant speed-of-sound c_0 of 1540 m/sec, attributed to soft tissue. As a result, the transducer records the echo at a different time than it would if the medium were truly homogeneous. The latency is described by the difference between Equation (1) and Equation (2):

$$dt = 2\int_0^z \frac{1}{c(z')} - \frac{1}{c_0} dz' \tag{3}$$

3.1.2 Imaging Applications

To create an image of the field of view, a series of pressure waves must be emitted, and their echoes recorded. In classical ultrasound, focused pressure waves are used to generate an ultrasound frame. When fired together, a sub-aperture of elements is fired together in harmony, generating a planar wave front. Instead, the sub-aperture can be dynamically focused by delaying the phase of transmission for each element to create a focal point, at which the acoustic intensity is maximal. Furthermore, the focal point can be electronically steered by adding a linear delay to the phase of each element. At the focal point, the coherent pressure waves induce a peak acoustic intensity, and the maximal signal-to-noise ratio (SNR) and resolution are achieved. Examples of such delay schemes can be seen in Figure 1.

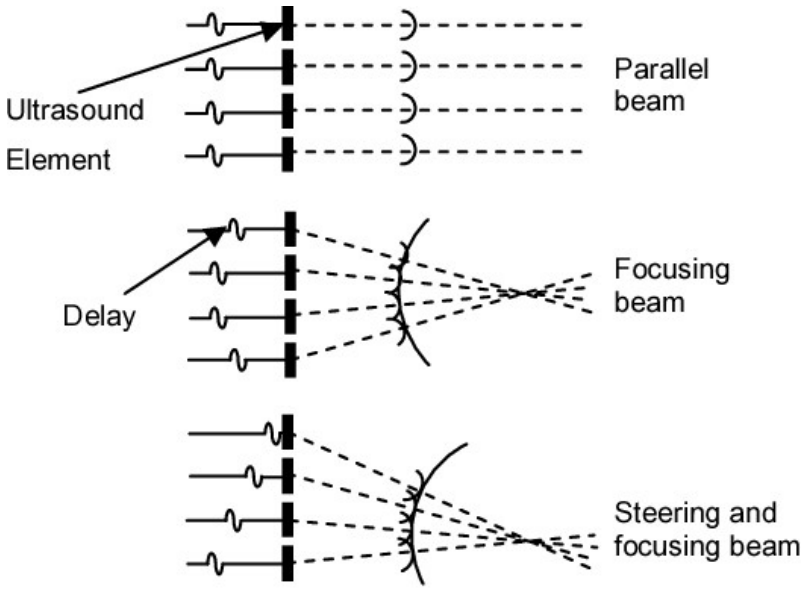

Figure 1. Schematic diagram of dynamic beam focusing in ultrasound. The pressure wave is induced in each element with a delay corresponding to its geometric location in the sub-aperture to create the desired focal point. A constant delay gives a parallel beam (plane wave), while a parabolic delay pattern creates a focal point. Additional linear delay can be added to steer the focal point. Diagram adapted from [20].

The recorded echo is received at the transducer surface and the amplitude is encoded and digitized as a function of time according to Equation (1). The acquired 1D signal is referred to as an A-line. Consecutive A-lines are acquired by sweeping the active region of the transducer across the full aperture, each time encoding an A-line perpendicular to the working sub-aperture. These A-lines are joined together to form a brightness-mode or B-mode ultrasound image.

However, the time of the delay required for such focusing is parabolic in nature and thus is of the same order as the effective frame rate. As a result, using such delays for full frame acquisition with hundreds of such steered and focused beams inhibits the frame rate of the ultrasound acquisition. Instead, coherent plane wave compounding can be implemented to maximize the temporal and spatial resolution simultaneously, often settling on a signal-to-noise

ratio to frame rate tradeoff of 50-500 frames/sec [21]. In plane wave compounding, very short linear delays are added to create an angled plane wave, usually fired from the entire transducer at once. Although plane waves are inherently unfocused, their linear delay time allows the rapid acquisition of many plane waves in a short amount of time, and they are added together to increase image coherence. This compounding scheme provides high SNR at very high frame rates. Figure 2 highlights the advantages of this setup as opposed to classical B-mode imaging.

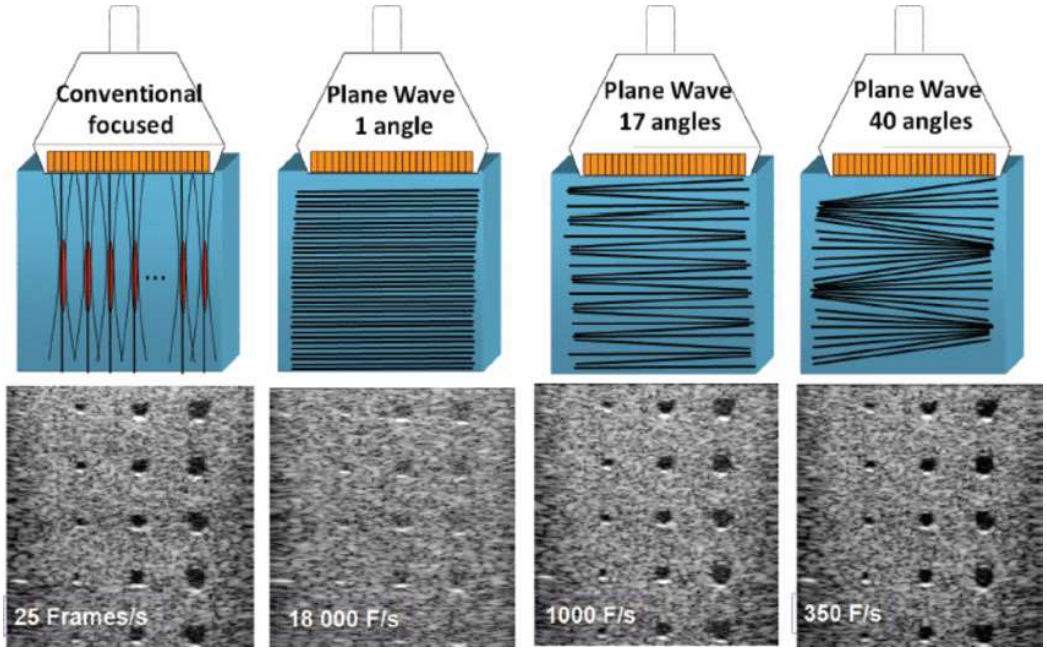

Figure 2. Schematic diagram of coherent plane wave compounding compared to classical B-mode imaging. Individual plane waves can be sampled much faster than focused A-lines, but at the cost of poor SNR and contrast. To overcome this, many plane waves are compounded together. Thus, imaging parameters are optimized but the effective frame rate is an order of magnitude higher. Diagram is adapted from [22].

Ultrasound imaging is usually performed at frequencies in the range of 1-20 MHz, and the pressure wave modulates an object in the viewing field- as such it is necessary to extract the signal envelope whose amplitude is eventually encoded to a pixel representing the object. Thus, after RF data is recorded at the transducer surface, it is Hilbert transformed to extract the

envelope, then delayed to account for the spherical propagation of waves echoed from reflectors in the tissue. This process is known as beamforming.

3.2 Therapeutic ultrasound

Therapeutic ultrasound utilizes concentrated ultrasound waves to generate therapeutic effects non-invasively. Conceptually, single-element HIFU is similar to optical focusing of light through a lens. A large, spherical, single-element transducer fires high intensity sound waves geometrically focused to a single point. This induces a strong, localized mechanical vibration of tissue at the focal site. As the tissue vibrates, energy is released, heating the target area. It is important to note that the tissue between the transducer and focal site is not heated, as the acoustic power is only coherently increased at the focus.

Hyperthermia and thermal ablation procedures are performed by applying HIFU at increasing frequency, duty cycle, and acoustic output power. In hyperthermia, a thermal window of 41-45º Celsius is targeted, while more intense thermal ablation techniques apply HIFU at temperatures in excess of 50º C [23]. Based on the goal of a HIFU procedure, a different operating temperature may be appropriate. Table 1 indicates the effect of different temperature windows on the human body.

Temperature range (°C)	Effects
37-39	Extended exposure has no harmful impact.
39-43	Over time, adverse effects may arise.
>41	Fetal issues may arise after extended periods of exposure.
44-46	Protein coagulates.
>45	Enzymes become denatured.
>41.8	Cancer cells fail to reproduce and die.
	This is generally considered a threshold for damage (except eye).

Table 1. Temperature effects. Adapted from [24].

3.3 Ultrasound Safety

In general ultrasound is a safe imaging procedure due to the non-ionizing nature of acoustic waves. However, thermal effects of ultrasound as described above clearly suggest that permanent damage can be induced using sound waves.

The “thermal risk” of ultrasound systems is dependent on both temperature and time [25] . Longer sonification inducing higher temperature creates a larger energy release into the tissue. This is the primary difference between imaging and therapeutic ultrasound- therapeutic ultrasound emits focused pressure waves for several minutes at a time with high output power and duty cycle, while imaging protocols make use of lower energy sound waves complying with regulated parameters like the Thermal Index for Soft Tissue (TIS).

3.4 HIFU guidance

3.4.1 Current state-of-the-art

Today MR thermometry is the method of choice for HIFU guidance. MRI machines provide very high spatial resolution but suffer from severe drawbacks in terms of accessibility,

equipment compatibility, patient positioning, and treatment time. MRI machines are often large and expensive, limiting their availability in certain healthcare facilities. The strong magnetic fields generated by MRI can cause distortions in ultrasound beams, requiring specialized MRI-compatible HIFU systems for accurate targeting. Patient positioning inside the MRI scanner can be challenging due to the need for real-time adjustments and monitoring during HIFU treatments. Additionally, the combination of MRI and HIFU procedures can lead to longer overall treatment times, which may impact patient comfort and resource utilization. Moreover, MR thermometry cannot image the temperature change in fat [26], which is a risk factor in potentially fatty tissues like the breast and liver.

3.4.2 Thermal strain imaging

Ultrasonic monitoring of HIFU is based on the relationship between temperature and speed-of-sound. Several works by Ebbini [27]–[30] described how this relationship produces a measurable latency in the echo over successive ultrasound frames captured by an imaging transducer. Thus Equation 3 is revised to include the effects of heating:

$$\delta t = 2 \oint \frac{1 + \beta(z)\delta T}{c(z,\, T)} - \frac{1}{c(z,\, T_0)} dz \tag{4}$$

where the difference in round-trip time $\delta\tau$ is the cumulative sum of the inverse of changes in local sound speed c(z,T) due to a temperature change δT from the initial temperature T_0 in tissue with a thermal expansion coefficient of $\beta(z)$ along the wave propagation path. Originally, latency was measured by comparing the time it took for sound waves to cross the field of view, but this technique requires two transducers (a source and a receiver) [31]. Notable methods to calculate the echo shift are cross-correlation template matching as well as Loupas' Estimator, but these are computationally burdensome calculations [32].

In TSI, this integral is differentiated along the propagation path and several assumptions can be made to simplify the equation for calculation of temperature change from echo latency:

$$\frac{\partial}{\partial z}(\delta t) = \alpha_1 \times \delta T \tag{5}$$

where α_1 is a medium-specific parameter describing the thermal expansion coefficient and linear relationship of sound speed with temperature and can also be thought of as a unit conversion parameter from thermal strain to temperature. Phase aliasing artifacts common to typical ultrasound imaging methods must be filtered after the echo shift is calculated, often incorporating heavy filters such as the median filter or Savitzky-Golay. Such artifacts greatly impede the calculation of thermal strain from the echo shift measurement suggested in Equation (5). Thermal strain calculation is impartial to the underlying ultrasound acquisition method or heating procedure, and different imaging schemes have been implemented based on TSI, but these methods are still computationally expensive due to the calculation of echo shift by the TSI algorithm [14], [33]. Methods taking advantage of plane wave compounding [15] or GPU calculations [30] have already been used to speed up TSI, but they suffer from the same limitations. Other methods also based on the change in tissue properties have also been used in USgFUS, mostly based on the same algorithmic concepts [34].

Any method for ultrasonic estimation of temperature change from thermal strain based on Equation (5) will start by calibration of the constant α_1 using a known ground truth temperature sensor. In this work we will assume a linear relation between the speed-of-sound and the change in temperature because we are interested in improving the estimation of sound speed shift, which is the underlying cause of thermal strain, rather than the calibration to temperature measurements. For water-based soft tissue, the constant α_1 has been reported to be -0.1 % $°C^{-1}$ change in thermal strain for a 1°C increase in temperature [35].

Once the echo shift has been measured, it can be used to calculate the temperature change. In TSI, this is done by differentiating the echo shift in the axial direction to produce thermal strain, which can be directly calibrated to the temperature shift. The relationship between strain and temperature shift is assumed to be linear [36], though much work has been done to assess the validity of this assumption- concluding that the relationship between thermal strain and temperature change is actually quasi-linear [37] or almost linear [38], [39].

3.4.3 Proposed method

In our method, DSI, we suggest a new approach to measuring and solving Equation (4). Rather than use a heavy and sparse cross-correlation approach, we propose a dense optical flow algorithm for echo shift calculation. The method offers reduced computation time and increases spatial coherence leading to a precise temperature estimation. Calculating the echo shift is conceptually identical to pixel-tracking, and echo shift has already been calculated [40] using the Horn-Shunck Dense optical flow algorithm [41]. This approach has several advantages. First, this algorithm incorporates a spatial smoothness prior, forcing the resulting echo shifts to be spatially coherent as expected. In addition, dense optical flow can incorporate more intricate motion models than just translation and in many cases outperforms block matching algorithms [42]. Finally, optical flow algorithms utilize pyramid calculation schemes to incorporate both low and high resolution information quickly. Today, Gunnar Farneback's [43] algorithm based on polynomial expansion is widely used to attain fast, spatially coherent pixel-motion results. In our work, we will combine fast plane wave imaging with optical flow to calculate the echo shift along several steering angles in real time, providing additional information about the field of view.

Once the echo shift has been measured, we will choose not to differentiate the line integral as in Equation (5) as this once again ignores the spatial coherence of the HIFU therapy. Instead, we propose unifying echo shift information from several plane waves to predict the change in speed-of-sound using an inverse problem method regularized with a spatial smoothness prior, which can similarly be calibrated to yield the underlying temperature shift. Regularized inverse problem approaches have shown promising results in ultrasound applications related to sound speed [44], [45] in addition to additional methods based on the beam geometry [46], passive reflectors [47] or diverging waves [48].

To formulate the inverse problem approach, we first assume the problem to be linearizable. Therefore, Equation (4) can be vectorized. The integral is represented as a matrix, denoted M below and the following equation is obtained:

$$\Delta \underline{\mathrm{d}} = \mathrm{M}\, \Delta \underline{v} \tag{6}$$

where the pixel shift $\Delta \underline{\mathrm{d}}$ is observed in a plane wave B-mode image due to an echo shift of δt. This $\Delta \underline{\mathrm{d}}$ is the result of integrating the operand:

$$\Delta \underline{v} = \frac{1 + \beta(z)\delta T}{c(z,\, T)} - \frac{1}{c(z,\, T_0)} \tag{7}$$

Once the integral operand $\Delta \underline{\mathrm{v}}$ is isolated, it is equivalent to the derivative of (4) such that Equation (5) can be rewritten without the derivative to obtain:

$$\Delta \underline{v} = \alpha_2 \times \delta T \tag{8}$$

with α_2 assuming the tissue-dependent role of units conversion previously denoted in Equation (5) as α_1. In temperatures up to 40°C, the relationship between sound speed and temperature

change is mostly linear and α_2 should correspond to a change of up to 1 m/sec for a 1º C rise in temperature, depending on the target tissue [35].

In practice, we want to measure the pixel shift, calculate $\Delta\underline{v}$ and estimate the underlying temperature change, so the following inverse problem is formulated:

$$M^{-1}\Delta\underline{d} = \Delta\underline{v} \tag{9}$$

This problem is over-defined since many $\Delta\underline{d}$ images can be acquired from a particular field of view representing a single $\Delta\underline{v}$. After transmitting multiple angled plane waves into the target tissue, a Tikhonov pseudo-inverse is utilized to calculate the optimal $\Delta\underline{v}$ satisfying the data. While this increases the potential for a reliable result, we further incorporate a smoothness prior to ensure spatial coherence. We chose to regularize the spatial gradient in the axial, lateral, and diagonal directions using L2 regularization. Thus, the detected change in sound slowness $\Delta\underline{v}$ is estimated by solving the following least squares problem:

$$\Delta\underline{\hat{v}} = \operatorname{argmin}_{\Delta\underline{v}} \left|\Delta\underline{d} - M\,\Delta\underline{v}\right|^2 + \Gamma\left|\nabla(\,\Delta\underline{v})\right|^2 \tag{10}$$

The pipeline of our DSI method utilizes the acquisition of ultrasound plane wave B-Mode images (Figure 3). The pixel shift at consecutive time intervals for a particular steering angle is computed via optical flow to produce the measured $\Delta\underline{d}$ vector. This vector is inverted as an inverse problem to receive $\Delta\underline{v}$. Finally, the units of $\Delta\underline{v}$ are converted to temperature by a pre-calibrated constant. Our method combines the optical flow algorithm and inverse problem regularization to create a temperature estimating algorithm that can incorporate a wide array of information while forcing both the input and output to obey spatial regularization constraints.

Utilization of prior knowledge about the spatial coherence of the HIFU surgery provides a faster more robust result with no need for additional image processing.

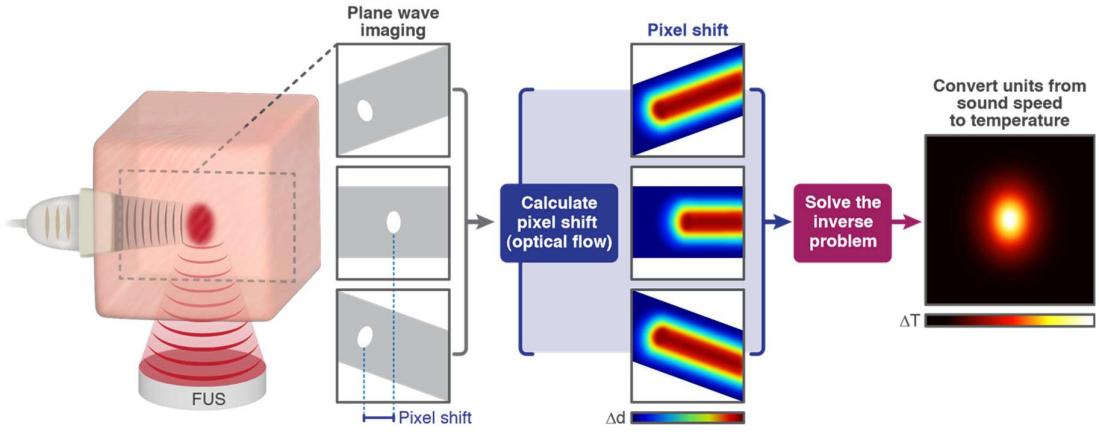

Figure 3. A schematic diagram describing the DSI algorithm. Ultrasound B-Mode images are acquired at various plane wave steering angles and the pixel shift at consecutive time intervals is computed. This produces the measured $\underline{\Delta d}$ vector which is inverted to receive $\underline{\Delta v}$. Finally, the units of $\underline{\Delta v}$ are converted to temperature by a pre-calibrated constant.

4. Materials and methods

4.1 Ultrasound setup

HIFU was performed with a 2 MHz spherically focused single element transducer (H107, Sonic Concepts, Bothell, WA, USA) that was controlled by a transducer power output unit (TPO-200, Sonic Concepts, Bothell, WA, USA). This transducer has a diameter of 64 mm and is focused at a depth of 45 mm. Each transmitted pulse consisted of a sinusoid with a peak negative pressure of 3.25 MPa and a duty cycle of 50%. These parameters matched standard hyperthermia experiments [15], [49]. To create a steady increase in temperature, the therapeutic transducer transmitted with a pulse repetition time of 20 µsec with bursts that consisted of 20 cycles. HIFU treatment was performed in intervals of 45 sec lasting a total duration of 270 sec. After every interval, imaging was performed and the results stored before the next HIFU cycle began.

The therapeutic transducer was placed face-up at the bottom of a custom water tank. A holder was located at the focal spot, where the sample was placed. Imaging was performed using an L12-5 50mm linear transducer (ATL Philips, WA, USA) placed perpendicular to the sample and coupled with ultrasound gel (Figure 4a). A programmable ultrasound system (Vantage 256, Verasonics Inc., WA, USA) was used for imaging of a 59 mm x 40 mm field of view. A plane steering acquisition protocol was used to acquire nine plane waves per imaging sequence. Three main steering angles were selected at 5° intervals [-5°, 0°, 5°], each composed of three steering angles selected at 1.5° intervals (for example [-6.5°, -5°, -3.5°]). Raw RF data was stored for offline processing.

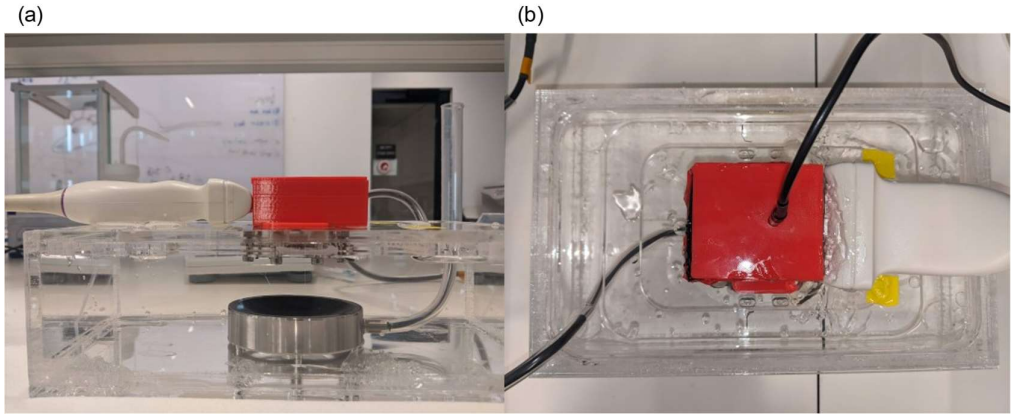

Figure 4. Experimental setup. (a) The imaging transducer is placed perpendicular to the sample, which is contained in a 3D printed cartridge at the focal point of the HIFU transducer, located at the bottom of a water tank. (b) ultrasound gel is added to couple the imaging transducer to the sample. A thermocouple is placed inside the sample to provide a ground-truth temperature reading.

Two types of samples were used. The first was a tissue mimicking phantom. The phantom was made by heating a combined mixture of 1% agarose powder (A10752, Alfa Aesar, MA, USA) with deionized water until boiling. 1% Silicon Carbide (57391, Sigma Aldrich, MO, USA) was added to the cooling mixture as acoustic scatterers, and the result was poured into a mold to congeal. Next, fresh ex-vivo chicken breast samples were used. Each chicken breast sample was cut from the thickest part of a chicken breast in a single piece that could fill the

entire field-of-view (pieces with a size of 59 mm x 40mm x 15 mm^3). The samples were placed in a 3D printed cartridge at the focal spot of the transducer. To minimize reflections 6 mm rubber was placed around the sample and coupled with ultrasound gel. As a ground truth reference, a thermocouple was placed near the focal spot. The probe was operated from MATLAB during the imaging sequence through an Arduino Uno R3 (Figure 4b).

The pressure amplitude in this setup was calibrated using a needle hydrophone (NH0500, Precision Acoustics, Dorchester, UK) with an active aperture of 0.5 mm connected to an oscilloscope (MDO3024, Tektronix, OR, USA). The hydrophone was placed at the focal spot of the therapeutic transducer, such that the measured amplitude was maximal in the x, y, and z directions.

4.2 Post-processing

RF data was beamformed, Hilbert transformed, and the 1.5° angled plane waves sub-sets were compounded such that each image acquisition provided three main steering angles. For example, the set [-6.5°, -5°, -3.5°] was compounded to yield a single image of -5°. This unique compounding has been used previously to enhance the signal-to-noise ratio in preparation for the pixel-tracking step [45]. The dense optic flow was calculated between consecutive images at each of the main steering angles using Farneback's method [43]. The three calculated pixel-shift images acquired at each time interval were down-sampled x5 in the lateral direction and x10 in the axial direction, then fed into the precalculated inverse model according to Equation (10) with regularization parameters $\Gamma x = 10$, $\Gamma z = \Gamma xz = 1$. The resulting image of pixel change in sound slowness was up-sampled back to the original image dimensions, then summed and compared to the expected temperature change to fit a linear curve, producing the calibration constant α_2.

As a reference to DSI, TSI was also computed using the same data sets. Implementation included a 1-D cross-correlation search algorithm along each plane wave's propagation axis based on [15]. The pixel shift was smoothed in the lateral direction with a Savitzky-Golay filter of length 13.4 mm and then the axial gradient was estimated with a second, gradient estimating Savitzky-Golay filter of length 15.6 mm. Each of the main angles described previously was analyzed separately, then the results were compounded for each time step.

Both algorithms were implemented in python. DSI's optical flow component made use of the OpenCV library, while the inverse problem solution was implemented as a sparse matrix multiplication using scipy. TSI, which requires a complex cross-correlation search, was implemented in numba as just-in-time compiled python code utilizing parallel processing to improve performance.

5. Results

5.1 Simulated data

To validate our method, a simulated pixel-shift was induced in a set of steered plane wave images acquired from agarose tissue-mimicking phantom. A circular lesion mimicking a heated area was simulated within the images by introducing a temperature shift of approximately 10 ^{o}C, at a circular area centered in the image with a radius of 5 mm (Figure 5). The ground truth model is presented alongside TSI thermal strain calculation and DSI slowness deviation reconstruction (Figure 5b,d, f, respectively). The pixel shift of the TSI method provides a lateral full-width at half-max (FWHM) of 8.19 mm, while the DSI method gives a FWHM of 8.79 mm. The ground truth lateral FWHM is 8.49 mm, which is closer to the DSI result. In terms of lesion dimensions, the lateral FWHM in TSI reconstruction is 10.56 mm while DSI achieves

9.57 mm. In the axial direction, TSI gives a FWHM of 7.89 mm while DSI gives 15.5 mm. The ground truth was 9.77 mm in each direction. Overall there is a smoother result with the DSI method.

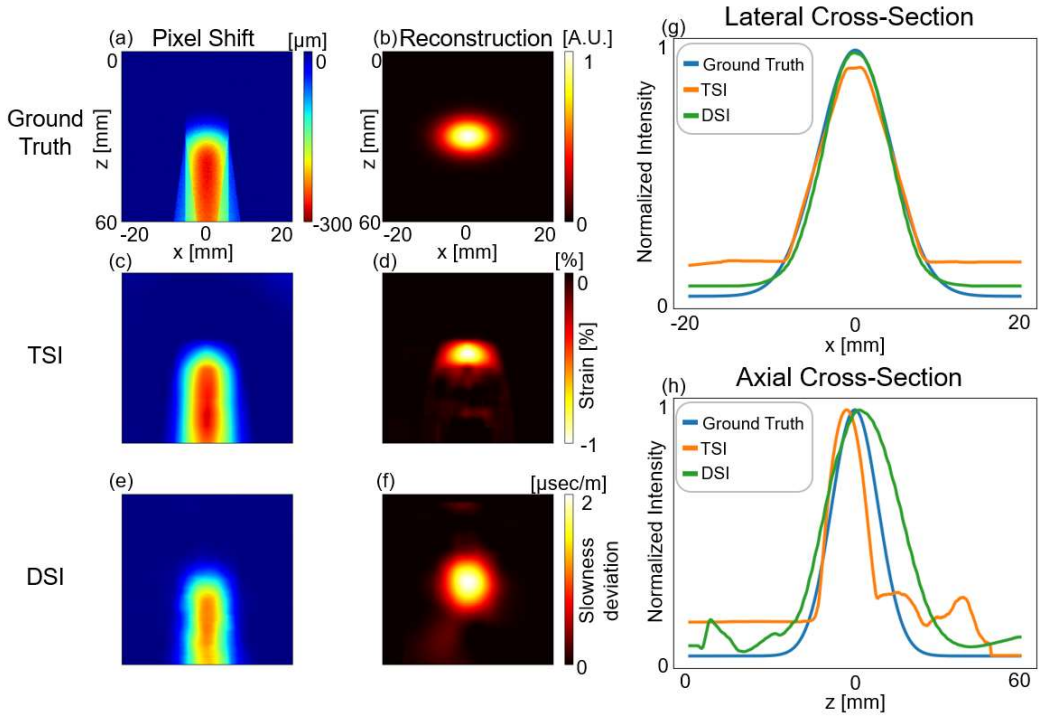

Figure 5. Simulation results. Pixel shift for (a) ground truth. (c) TSI, and (e) DSI methods. The reconstruction of the heated area is for (b) ground truth, (d) TSI, and (f) DSI methods. The reconstruction cross-sections are analyzed in the lateral (g) and axial (h) directions for the three methods. Axes are common to subfigures (a)-(f). Colorbar is common to subfigures (a), (c), (e).

5.2 Ex-vivo

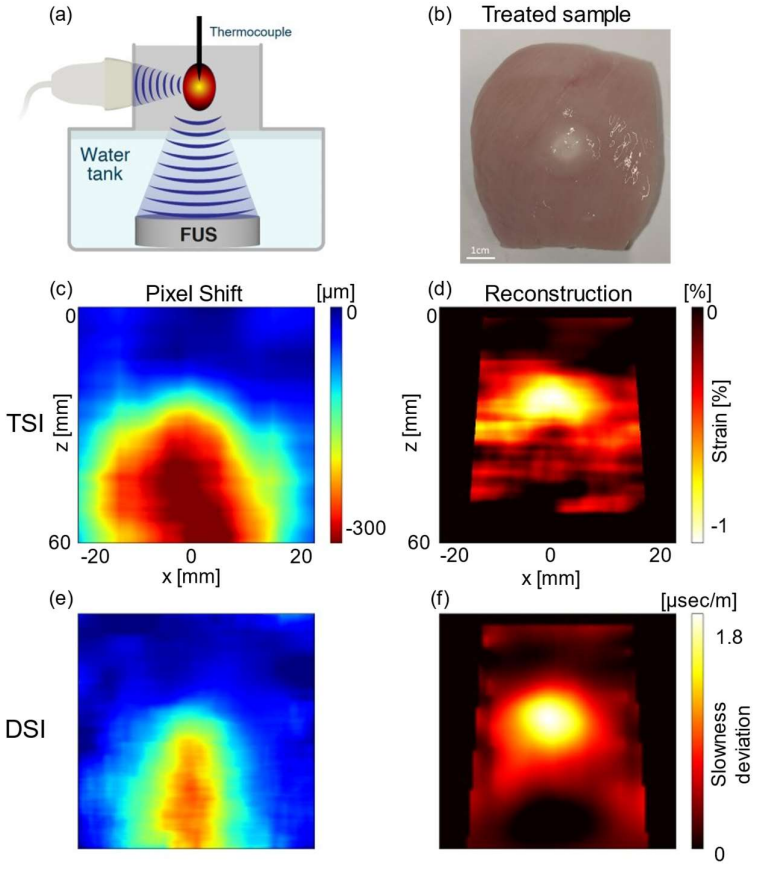

Figure 6. Experimental comparison between the TSI and DSI methods. (a) Experimental setup illustration. (b) Image of an ex-vivo chicken breast sample following a 270 sec ablation treatment. Pixel shifts result for the (c) TSI and (e) DSI methods after the first treatment. Treated region reconstruction of the pixel shift maps using (d) TSI and (f) DSI methods. Axes are common to subfigures (c)-(f). Colorbar is common to subfigures (c), (e).

Next, ex-vivo chicken breast experiments were conducted. HIFU was applied at the center of the sample, and an ablated region was visible at the center of the images of the sliced sample (Figure 6b). A thermocouple was located at the focal spot to serve as the ground truth measurement. The imaging array acquired plane waves on the transversal plane of the sample. The recorded pixel shift and the reconstructed image were compared between the TSI and DSI

methods (Figure 6). The lesion detected with TSI has a focal area of 226 mm² (Figure 6d) while the DSI lesion recorded a focal area of 177 mm².

Next, the effect of the HIFU duration on the DSI algorithm performance was assessed (Figure 7). Larger speed of sound shift was observed with an increase in treatment duration. The detected slowness deviation and focal area for each time step was assessed across six experiments and are displayed in Table 2.

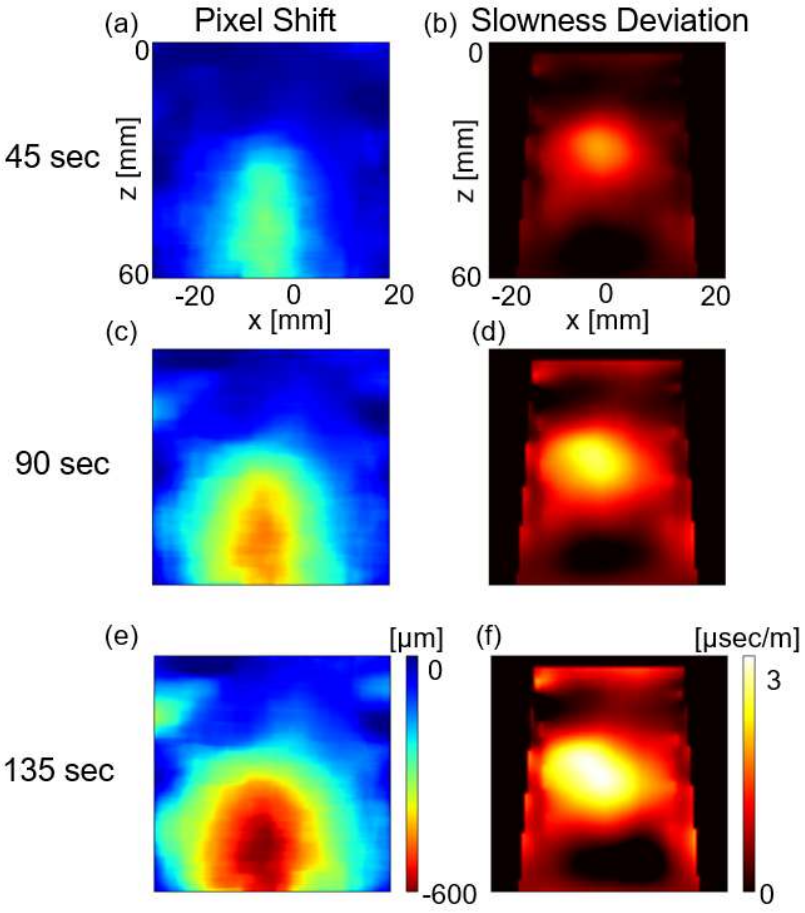

Figure 7. Effect of treatment duration on the DSI algorithm. HIFU treatment was conducted for 45, 90 or 135 sec, yielding the pixel shifts (a), (c), and (e), respectively and the sound slowness (b), (d), (f). Axes are common to all subfigures. Colorbar is common to subfigures (a), (c), (e) and (b), (d), (f).

Treated region area increased by 42% for 90 sec compared to 45 sec, and by 75% for 135 sec treatment (Table 2).

Treatment Time [sec]	Max slowness Deviation [μsec/m]	Measured focal area [mm²]
45	1.2 ± 0.4	174.5 ± 53.6
90	1.7 ± 0.5	221.8 ± 51.5
135	2.1 ± 0.6	252.6 ± 69.4

Table 2. Detected slowness deviation and focal area of the treatment spot across experiments.

5.3 Temperature estimation

After repeating the experiment presented in Figure 7 six times, the mean temperature for each treatment interval was calculated. The average thermocouple measurements were used as a ground-truth model to represent the expected change in temperature. Sound slowness and thermal strain were extracted from the DSI and TSI algorithms respectively and calibrated to the ground truth model. Calibration of the temperature profiles yielded values of -0.22 % $^{o}C^{-1}$ for α_1 and 88 ηsec/m $^{o}C^{-1}$ for α_2, corresponding to a change of 0.3 m/sec for a 1 ^{o}C temperature increase. These values were used for calculating the temperature prediction (Figure 8).

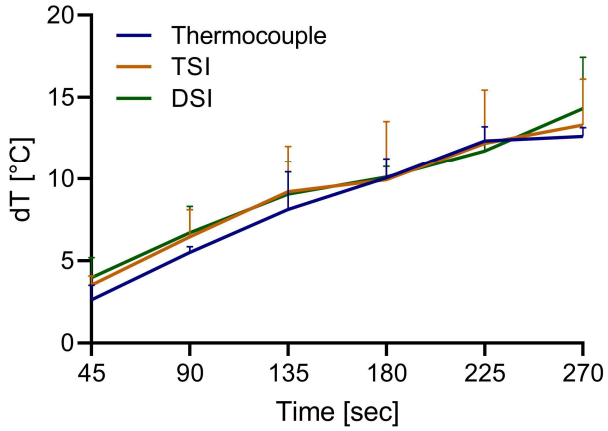

Figure 8. Comparison of Temperature estimation as a function of HIFU duration (N=6 samples). Ground truth thermocouple measurements (blue line), TSI (orange line), and DSI (green line). Results are presented as mean ± STD.

5.4 Performance benchmark

Finally, to emphasize the improvement in temporal resolution of the DSI algorithm, we performed a bench test to determine the average runtime of the algorithm compared to TSI. The cross-correlation parameters used in the search algorithm were chosen to optimize imaging quality as in Figure 6. Four random experiments were selected, and each was processed 100 times with each algorithm. The processing time for each iteration was divided by the number of frames to calculate the mean time per frame. The average runtime of the TSI algorithm was 7.21 ± 0.5 sec/frame, while DSI ran in 0.33 ± 0.004 sec/frame. Overall, a speedup of x20 was achieved with DSI.

6. Discussion

In this paper we developed a method for imaging a local speed-of-sound shift with a dense algorithm for the purpose of temperature estimation, aiming to improve the calculation time and spatial coherence of the result. The proposed DSI algorithm is robust and could be

used to monitor additional applications that induce a speed-of-sound shift. The common method for ultrasonic thermometry is TSI which is based on a cross-correlation search and local axial gradient. Our experiments showed several promising advantages for the DSI algorithm in HIFU guidance compared to TSI. First, across all experiments, it is clear that the smoothness priors used in the optical flow calculation and inverse problem regularization greatly improve the spatial coherence of the results. This is captured in Figure 6, where the image processing steps that work well in the simulated TSI results do not generalize well to ex-vivo, and the TSI pixel shift estimation gives a large focal area. In Figure 6, heavy smoothing was necessary to reach an adequately smooth TSI image. One of the main advantages of DSI is not needing the additional filtering. In the future, knowledge of the shape of a HIFU beam in the transverse imaging plane can intuitively incorporate further apriori information into the DSI inverse problem solution to produce a more complex regularization scheme. This improvement can be further capitalized on by increasing the amount of plane waves to more heavily oversample the sound slowness field. Both of these concepts can be used to reduce the blurring caused by trivial L2 spatial regularization (Figure 5h).

Another notable benefit of the DSI algorithm is its runtime. TSI and other correlation-based tracking methods are insufficient for real-time use when the region of interest is the entire frame. In this case it is preferable to make use of dense algorithms incorporating all of the available information simultaneously, while eliminating the need for image processing. Removal of the search step of TSI and replacement with optical flow provided a large part of the performance boost, but DSI's slowness estimation is also very fast due to the use of largely sparse matrices in solving the inverse problem. In ex-vivo samples we detected a slowness deviation in order of 3 μsec/m, which corresponds to a sound speed change of 7m/sec from a base sound speed of 1540 m/sec. This translates to a speed-of-sound change of 0.45%. The

temperature estimation results were similar between the ground truth thermocouple measurements, the TSI and DSI methods (Figure 8).

There are a number of limitations that should be mentioned. First, as in any ultrasound-based technique, the speed-of-sound shift can be measured only in soft tissue. In cases where the ablated region is located within bone, such as in transcranial ablation, MRI thermometry remains superior. In addition, there is variability in temperature measurements that can be attributed to several factors (Figure 8). Here the relationship between tissue temperature and sound speed change was modelled as a scalar unit conversion, but in practice it is a tissue-dependent curve that is linear only for certain temperature ranges [35], [37] however this is not a new issue in our algorithm but rather a known drawback of temperature estimation methods based on Equation (4). In the experiments described above we have performed only HIFU-induced hyperthermia treatments and taken care to stay within the linear region of this curve, but in thermal ablation therapy this temperature range is often crossed and the linearity is compromised. So long as the linear temperature region is maintained, we believe our algorithm can also be extended to more aggressive treatments such as thermal ablation therapy, at least as well as TSI. Another issue with temperature calibration are the absorptive and viscous heating artifacts common to thermocouples [37], [50]. As the tissue vibrates under the effect of HIFU, friction is generated between the tissue and the thermocouple, introducing viscous heat that is not present in true surgical HIFU applications. Additionally, the thermocouple itself absorbs heat from the surrounding tissue. Thus, temperature calibration of slowness deviation is forced to overcompensate for this heat in the thermocouple. Moreover, temperature calibration depends on the thermocouple positioning. A shift in positioning will add a built-in error to the process. Last, the heavy noise present in ultrasound imaging often confounds algorithmic applications, and both TSI and DSI are no exception. The estimation of echo delay

is greatly impacted by the noise levels, and each algorithm has a different method of compensating. It is possible to further fine-tune these steps (image processing, or dense estimation) but we see the current implementation as a reasonable tradeoff between image quality and runtime. Finally, there is an important balance between spatial regularization and resolution. Here we have opted to introduce strong regularization, and Figure 6 shows that this is preferable to the image processing done in TSI, but at the cost of spatial resolution.

Despite these difficulties, error in temperature measurement is as good as that of TSI, largely due to the high accuracy of the slowness deviation estimation. Our algorithm can provide reasonable, robust slowness deviation estimation in real-time applications, and more work can be done on the calibration to temperature for HIFU guidance. The algorithm can be implemented in real-time as shown by the performance benchmark, by storing the pseudo-inverse matrix, beamforming each plane wave angle independently, tracking the pixel motion, and solving the inverse problem with a simple matrix multiplication. We believe that the speed up in the algorithm run time could facilitate its implementation as part of a closed-loop HIFU controller or be used with matrix array transducers to enable real-time 3D thermometry.

7. References

[1] C. X. Li *et al.*, "Analysis of clinical effect of high-intensity focused ultrasound on liver cancer," *World J. Gastroenterol.*, 2004, doi: 10.3748/wjg.v10.i15.2201.

[2] L. Poissonnier *et al.*, "Control of Prostate Cancer by Transrectal HIFU in 227 Patients," *Eur. Urol.*, vol. 51, no. 2, pp. 381–387, Feb. 2007, doi: 10.1016/J.EURURO.2006.04.012.

[3] F. Wu *et al.*, "A randomised clinical trial of high-intensity focused ultrasound ablation for the treatment of patients with localised breast cancer," *Br. J. Cancer*, 2003, doi: 10.1038/sj.bjc.6601411.

[4] J. W. Chang, B. K. Min, B. S. Kim, W. S. Chang, and Y. H. Lee, "Neurophysiologic Correlates of Sonication Treatment in Patients with Essential Tremor," *Ultrasound Med. Biol.*, 2015, doi: 10.1016/j.ultrasmedbio.2014.08.008.

[5] W. J. FRY, W. H. MOSBERG, J. W. BARNARD, and F. J. FRY, "Production of focal destructive lesions in the central nervous system with ultrasound," *J. Neurosurg.*, 1954, doi: 10.3171/jns.1954.11.5.0471.

[6] E. Maloney and J. H. Hwang, "Emerging HIFU applications in cancer therapy," *International Journal of Hyperthermia*. 2015. doi: 10.3109/02656736.2014.969789.

[7] S. Moosa, R. Martínez-Fernández, W. J. Elias, M. del Alamo, H. M. Eisenberg, and P. S. Fishman, "The role of high-intensity focused ultrasound as a symptomatic treatment for Parkinson's disease," *Movement Disorders*. 2019. doi: 10.1002/mds.27779.

[8] M. D. Gray *et al.*, "Focused ultrasound hyperthermia for targeted drug release from thermosensitive liposomes: Results from a phase i trial," *Radiology*, 2019, doi: 10.1148/radiol.2018181445.

[9] A. N. Guthkelch *et al.*, "Treatment of malignant brain tumors with focused ultrasound hyperthermia and radiation: results of a phase I trial," *J. Neurooncol.*, 1991, doi: 10.1007/BF00177540.

[10] M. B. Karmacharya, L. R. Sultan, S. J. Hunt, and C. M. Sehgal, "Hydralazine augmented ultrasound hyperthermia for the treatment of hepatocellular carcinoma," *Sci. Rep.*, 2021, doi: 10.1038/s41598-021-94323-0.

[11] R. Staruch, R. Chopra, and K. Hynynen, “Localised drug release using MRI-controlled focused ultrasound hyperthermia,” *Int. J. Hyperth.*, 2011, doi: 10.3109/02656736.2010.518198.

[12] Y. S. Kim, “Advances in MR image-guided high-intensity focused ultrasound therapy,” *International Journal of Hyperthermia*, vol. 31, no. 3. Informa Healthcare, pp. 225–232, May 01, 2015. doi: 10.3109/02656736.2014.976773.

[13] A. Ilovitsh, B. Z. Fite, T. Ilovitsh, and K. W. Ferrara, “Acoustic radiation force imaging using a single-shot spiral readout,” *Phys. Med. Biol.*, vol. 64, no. 12, p. 125004, Jun. 2019, doi: 10.1088/1361-6560/ab1e21.

[14] J. Foiret and K. W. Ferrara, “Spatial and Temporal Control of Hyperthermia Using Real Time Ultrasonic Thermal Strain Imaging with Motion Compensation, Phantom Study,” 2015, doi: 10.1371/journal.pone.0134938.

[15] F. F. Lee *et al.*, “Evaluating HIFU-mediated local drug release using thermal strain imaging: Phantom and preliminary in-vivo studies,” *Med. Phys.*, vol. 46, no. 9, pp. 3864–3876, Sep. 2019, doi: 10.1002/MP.13719.

[16] D. Schein, T. Grutman, and T. Ilovitsh, “Deep Learning-Based Ultrasound Beam Shaping for Spatiotemporal Acoustic Holograms Generation,” *IEEE Trans. Ultrason. Ferroelectr. Freq. Control*, vol. 70, no. 6, pp. 551–561, 2023, doi: 10.1109/TUFFC.2023.3264580.

[17] K. T. Karlinsky and T. Ilovitsh, “Ultrasound Frequency Mixing for Enhanced Contrast Harmonic Imaging of Microbubbles,” *IEEE Trans. Ultrason. Ferroelectr. Freq. Control*, 2022, doi: 10.1109/TUFFC.2022.3179471.

[18] R. Abiteboul and T. Ilovitsh, “Optimized Simultaneous Axial Multifocal Imaging via Frequency Multiplexed Focusing,” *IEEE Trans. Ultrason. Ferroelectr. Freq. Control*, 2022, doi: 10.1109/TUFFC.2022.3200468.

[19] J. Foiret, H. Zhang, T. Ilovitsh, L. Mahakian, S. Tam, and K. W. Ferrara, “Ultrasound localization microscopy to image and assess microvasculature in a rat kidney,” *Sci. Rep.*, vol. 7, no. 1, pp. 1–12, 2017, doi: 10.1038/s41598-017-13676-7.

[20] M. T. Tan, C. M. Chu, and S. Chauhan, “High intensity ultrasound phased array for surgical applications,” 2006. doi: 10.1109/ICBPE.2006.348658.

[21] G. Montaldo, M. Tanter, J. Bercoff, N. Benech, and M. Fink, “Coherent plane-wave

compounding for very high frame rate ultrasonography and transient elastography," *IEEE Trans. Ultrason. Ferroelectr. Freq. Control*, vol. 56, no. 3, pp. 489–506, 2009, doi: 10.1109/TUFFC.2009.1067.

[22] M. Tanter and M. Fink, "Ultrafast imaging in biomedical ultrasound," *IEEE Trans. Ultrason. Ferroelectr. Freq. Control*, 2014, doi: 10.1109/TUFFC.2014.2882.

[23] P. R. Stauffer and S. N. Goldberg, "Introduction: Thermal ablation therapy," *Int. J. Hyperth.*, 2004, doi: 10.1080/02656730400007220.

[24] T. L. Szabo, *Diagnostic Ultrasound Imaging: Inside Out*. 2004. doi: 10.1055/s-2005-861725.

[25] T. A. Bigelow *et al.*, "The Thermal Index," *J. Ultrasound Med.*, 2011, doi: 10.7863/jum.2011.30.5.714.

[26] J. Blackwell *et al.*, "Proton Resonance Frequency Shift Thermometry: A Review of Modern Clinical Practices," *Journal of Magnetic Resonance Imaging*. 2022. doi: 10.1002/jmri.27446.

[27] R. Seip and E. S. Ebbini, "Noninvasive Estimation of Tissue Temperature Response to Heating Fields Using Diagnostic Ultrasound," 1995. doi: 10.1109/10.398644.

[28] C. Simon, P. Vanbaren, and E. S. Ebbini, "Two-dimensional temperature estimation using diagnostic ultrasound," *IEEE Trans. Ultrason. Ferroelectr. Freq. Control*, vol. 45, no. 4, pp. 1088–1099, 1998, doi: 10.1109/58.710592.

[29] D. Liu and E. S. Ebbini, "Real-time 2-D temperature imaging using ultrasound," *IEEE Trans. Biomed. Eng.*, vol. 57, no. 1, pp. 12–16, Jan. 2010, doi: 10.1109/TBME.2009.2035103.

[30] E. S. Ebbini, C. Simon, and D. Liu, "Real-Time Ultrasound Thermography and Thermometry [Life Sciences]," *IEEE Signal Process. Mag.*, 2018, doi: 10.1109/MSP.2017.2773338.

[31] C. M. Sehgal, G. M. Brown, R. C. Bahn, and J. F. Greenleaf, "Measurement and use of acoustic nonlinearity and sound speed to estimate composition of excised livers," *Ultrasound Med. Biol.*, vol. 12, no. 11, pp. 865–874, Nov. 1986, doi: 10.1016/0301-5629(86)90004-9.

[32] T. Loupas, R. W. Gill, and J. T. Powers, "An Axial Velocity Estimator for Ultrasound Blood Flow Imaging, Based on a Full Evaluation of the Doppler Equation by Means of a Two-Dimensional Autocorrelation Approach," *IEEE Trans. Ultrason. Ferroelectr. Freq. Control*, vol. 42, no. 4, pp. 672–688, 1995, doi: 10.1109/58.393110.

[33] X. Ding *et al.*, “Improved Estimation of Ultrasound Thermal Strain Using Pulse Inversion Harmonic Imaging,” *Ultrasound Med. Biol.*, vol. 42, no. 5, pp. 1182–1192, May 2016, doi: 10.1016/j.ultrasmedbio.2016.01.007.

[34] E. Shaswary *et al.*, “Real-time non-invasive control of tissue temperature using high-frequency ultrasonic backscattered energy,” 2021. doi: 10.1109/IUS52206.2021.9593438.

[35] C. H. Seo, Y. Shi, S. W. Huang, K. Kim, and M. O’Donnell, “Thermal strain imaging: A review,” *Interface Focus*. 2011. doi: 10.1098/rsfs.2011.0010.

[36] N. R. Miller, J. C. Bamber, and P. M. Meaney, “Fundamental limitations of noninvasive temperature imaging by means of ultrasound echo strain estimation,” *Ultrasound Med. Biol.*, 2002, doi: 10.1016/S0301-5629(02)00608-7.

[37] J. Civale *et al.*, “Calibration of ultrasound backscatter temperature imaging for high-intensity focused ultrasound treatment planning,” *Ultrasound Med. Biol.*, 2013, doi: 10.1016/j.ultrasmedbio.2013.04.001.

[38] U. Techavipoo, T. Varghese, Q. Chen, T. A. Stiles, J. A. Zagzebski, and G. R. Frank, “Temperature dependence of ultrasonic propagation speed and attenuation in excised canine liver tissue measured using transmitted and reflected pulses,” *J. Acoust. Soc. Am.*, 2004, doi: 10.1121/1.1738453.

[39] T. Varghese and M. J. Daniels, “Real-time calibration of temperature estimates during radiofrequency ablation,” *Ultrason. Imaging*, 2004, doi: 10.1177/016173460402600305.

[40] B. M. Mehrabani, V. Tavakoli, M. D. Abolhassani, J. Alirezaie, and A. Ahmadian, “An efficient temperature estimation using optical-flow in ultrasound B-Mode digital images,” *Proc. 30th Annu. Int. Conf. IEEE Eng. Med. Biol. Soc. EMBS’08 - "Personalized Healthc. through Technol.*, pp. 86–89, 2008, doi: 10.1109/IEMBS.2008.4649097.

[41] B. K. P. Horn and B. G. Schunck, “Determining optical flow,” *Artif. Intell.*, 1981, doi: 10.1016/0004-3702(81)90024-2.

[42] J. De Boer and M. Kalksma, “Choosing between optical flow algorithms for UAV position change measurement,” *Sc@ Rug*, 2015.

[43] G. Farnebäck, “Two-frame motion estimation based on polynomial expansion,” *Lect. Notes Comput. Sci. (including Subser. Lect. Notes Artif. Intell. Lect. Notes Bioinformatics)*, vol. 2749,

pp. 363–370, 2003, doi: 10.1007/3-540-45103-x_50.

[44] T. Robins, J. Camacho, O. C. Agudo, J. L. Herraiz, and L. Guasch, “Deep-learning-driven full-waveform inversion for ultrasound breast imaging,” *Sensors*, 2021, doi: 10.3390/s21134570.

[45] P. Stähli, M. Kuriakose, M. Frenz, and M. Jaeger, “Improved forward model for quantitative pulse-echo speed-of-sound imaging,” *Ultrasonics*, vol. 108, Dec. 2020, doi: 10.1016/J.ULTRAS.2020.106168.

[46] T. Brevett, S. J. Sanabria, R. Ali, and J. Dahl, “Speed of Sound Estimation at Multiple Angles from Common Midpoint Gathers of Non-Beamformed Data,” 2022. doi: 10.1109/IUS54386.2022.9958779.

[47] S. J. Sanabria, M. B. Rominger, and O. Goksel, “Speed-of-Sound Imaging Based on Reflector Delineation,” *IEEE Trans. Biomed. Eng.*, 2019, doi: 10.1109/TBME.2018.2881302.

[48] R. Rau, D. Schweizer, V. Vishnevskiy, and O. Goksel, “Speed-of-sound imaging using diverging waves,” *Int. J. Comput. Assist. Radiol. Surg.*, 2021, doi: 10.1007/s11548-021-02426-w.

[49] S. Park, N. T. Pham, H. T. Huynh, and H. W. Kang, “Development of temperature controller-integrated portable HIFU driver for thermal coagulation,” *Biomed. Eng. Online*, 2019, doi: 10.1186/s12938-019-0697-3.

[50] H. Morris, I. Rivens, A. Shaw, and G. Ter Haar, “Investigation of the viscous heating artefact arising from the use of thermocouples in a focused ultrasound field,” *Phys. Med. Biol.*, 2008, doi: 10.1088/0031-9155/53/17/020.

8. תקציר

במחקר זה, פתחנו אלגוריתם לחישוב שינוי במהירות קול בין תמונות אולטרסאונד עוקבות. השיטה פותחה על מנת להעריך את שינוי הטמפרטורה המקומי שנוצר במהלך טיפול של אבלציה תרמית לחימום הרקמה באופן לא פולשני. האלגוריתם לחישוב השינוי במהירות הקול (DSI) לוקח בחשבון מידע מכלל אזור העניין בעזרת שילוב של זרימה אופטית אינטגרלית ורגולריזציה של הבעיה ההפוכה המתקבלת. בצורה כזו ניתן לאלץ הסכמה בין פיקסלים שכנים באופן טבעי כדי ליצור תמונה חלקה יותר שמאפשרת ניטור של הטיפול וכן להאיץ את זמן החישוב. השיטה מורכבת משני שלבים עיקריים: עקיבה אחרי פיקסלים בעזרת זרימה אופטית בשיטת פרנבאק, ולאחר מכן מידול מתמטי של הקשר בין תזוזת פיקסל לשינוי הטמפרטורה כבעיה הפוכה למציאת השינוי שנוצר במהירות הקול כתוצאה מהחימום. קבוע כיול ממיר את התוצאה משינוי במהירות קול לשינוי בטמפרטורה. השיטה נבחנה בדוגמאות של חזה עוף וביצועי האלגוריתם החדש הושוו לשיטה הסטנדרטית בתחום, TSI. לאורך הניסויים, חיישן טמפרטורה שימש כרפרנס. האלגוריתם מומש על ידי מתמר הדמיה L12-5 שנשלט באמצעות מערכת אולטרסאונד מיתכנתת לצורך ניטור טיפול אבלציה תרמית בחזה עוף. שינויי טמפרטורה בין 3-15 מעלות צלזיוס נמדדו עם שגיאה של פחות מ2 מעלות עבור שינויי טמפרטורה של 8 מעלות ומעלה. שיטת הDSI התעלתה על פני שיטת הTSI הן מבחינת הקוהרנטיות המרחבית והן בזמן הריצה של האלגוריתם. לסיכום, השיטה שפותחה יכולה להעריך את שינוי המהירות קול שנגרם על ידי טיפול אבלציה תרמיתבצורה מהירה ויעילה יותר מהשיטות הקיימות כיום. אנו צופים שניתן יהיה להשתמש בשיטה בקליניקה לצורך ניטור זול, מהיר ולא פולשני של טיפולים תרמיים בזמן אמת.

אוניברסיטת תל אביב

הפקולטה להנדסה ע"ש איבי ואלדר פליישמן

בית הספר לתארים מתקדמים ע"ש זנדמן-סליינר

תרמומטריה אולטרסונית

חיבור זה הוגש כעבודת גמר לקראת התואר "מוסמך אוניברסיטה" בהנדסה ביו-רפואית

על-ידי

טל גרוטמן

העבודה נעשתה במחלקה להנדסה ביו-רפואית

בהנחיית ד"ר טלי אילוביץ

אוניברסיטת תל אביב

הפקולטה להנדסה ע"ש איבי ואלדר פליישמן

בית הספר לתארים מתקדמים ע"ש זנדמן-סליינר

תרמומטריה אולטראסונית

חיבור זה הוגש כעבודת גמר לקראת התואר "מוסמך אוניברסיטה" בהנדסה ביו-רפואית

על-ידי

טל גרוטמן

העבודה נעשתה במחלקה להנדסה ביו-רפואית

בהנחיית ד"ר טלי אילוביץ